Int. J. Electrochem. Sci., 12 **(2017)** 2429 – 2440, doi: 10.20964/2017.03.15

International Journal of
ELECTROCHEMICAL
SCIENCE
www.electrochemsci.org

Nano MoO_3 Phase Structural Evolution During Hydrothermal Synthesis and Its Electrochemical Properties

Li Jiwen[1], *Wei Shizhong*[1,2], *ZHANG Guo-shang*[1], *XU Liujie*[1,2], *Liu Wei*[1], *Pan Kunming*[2]

[1] Material Science & Engineering School, Henan University of Science & Technology, Luoyang 471023, China
[2] Henan Engineering Research Center for Wear of Materials, Henan University of Science & Technology, Luoyang 471003, China
*E-mail: ljwzq@haust.edu.cn

Received: 9 July 2016 / *Accepted:* 29 December 2016 / *Published:* 12 February 2017

Micron rods of hexagonal MoO_3 (h-MoO_3) and nanobelts of orthorhombic MoO_3 (α-MoO_3) were prepared using a facile hydrothermal synthesis. The factors that influenced the morphologies, crystalline structures and electrochemical properties of the MoO_3 were investigated by X-ray diffraction (XRD), scanning electron microscopy (SEM) and transmission electron microscopy (TEM). The experimental revealed that both the reaction time and acidity coefficient played important roles in controlling the crystalline structure and morphology of the MoO_3; however, the acidity coefficient was the crucial factor. At lower acidity coefficient, the growth of the MoO_3 nucleus only resulted in well-crystallized h-MoO_3 rods as the reaction time increased. As the acidity coefficient increased, the h-MoO_3 phase was transformed into an α-MoO_3 phase and the morphology changed gradually from three-dimensional hexagonal micron rods to low-dimension nanobelts. As the anode electrode, the α-MoO_3 nanobelts exhibited better electrochemical properties. The initial specific capacities of 223.1 $mAh \bullet g^{-1}$ and a wide discharge plateau of 2.2V for the α-MoO_3 were obtained. On the other hand a stable electrochemical performance was achieved for h-MoO_3 micron rods.

Keywords: hydrothermal synthesis; h-MoO_3 micron rods; α-MoO_3 nanobelts; reaction time; acidity coefficient; electrochemical properties

1. INTRODUCTION

Molybdenum oxide (MoO_3) is a polymorphous material that exhibits three basic structures. Orthorhombic MoO_3 (α-MoO_3) is thermodynamically stable, while monoclinic MoO_3 (β-MoO_3) and hexagonal MoO_3 (h-MoO_3) are metastable. The α-MoO_3 is considered to be a layered structure with Pbnm symmetry group composing of $[MoO_6]^{6-}$ octahedral units. The asymmetrical $[MoO_6]^{6-}$

octahedrons are interconnected through a corner link along the [001] face and exhibit edge sharing along the [001] face to form a double-layer sheet parallel to the (010) plane. Monoclinic β-MoO_3 has a ReO_3-related structure, in which the MoO_6 octahedra shares corner form a distorted cube. The h-MoO_3 material is also constructed in the same zigzag chains of the MoO_6 octahedra, but they are connected through the cis-position between chains [1-3]. Several reports have focused on the α-MoO_3, because α-MoO_3 not only has intensive active reactivity but also can decrease the path length for Li-ion transportation and increase interfacial contact area with electrolyte. So, α-MoO_3 is a kind of crystal with high energy density electrode material for rechargeable lithiumion battery and its theoretical electrochemical capacity is up to 670 $mAh\cdot g^{-1}$[4-6]. Although h-MoO_3 is suitable for insertion and extraction of the small ions, thanks to the tetrahedral and octahedral cavities in the lattice structure and the size of the structural channels [7-9], the electrochemical properties of this material have rarely been reported.

Unfortunately, α-MoO_3 cannot reach its theoretical capacity because of poor intrinsic physical properties predominantly with regard to ion transport and structural stability as well poor electronic conductors [10, 11]. In generally, the electrochemical performances of the electrode materials are not only related to the crystal structure, but also to the particles size and morphology of electrode materials. In order to overcome this problem, some of effective ways have been made, which employed different synthesis techniques and electrode fabrication process to improve active particle chemical composition, morphologies, size and usage of suitable amounts of electronic conducting materials [12]. A number of reports on the synthesis of MoO_3 have claimed a well-crystallized MoO_3 product using high processing temperature, prolonged processing time, microwave assistance or an electromagnetic stirring technique [13-15]. Gao [16] reported that the CTAB played a key role in the formation of α-MoO_3 nanobelts and the aspect ratio of nanobelts significantly varied with quality of CTAB. Using triblock copolymer as a dispersing agent by sol–gel method, Zhang [17] synthesized the α-MoO_3 nanoparticles, which showed the higher discharge capacity. Uttam [18] found that the selection of inorganic acid for MoO_3 preparation played an important role on the shape and size of the final product.

In this reported study, a facile hydrothermal method without any dispersing additive was used to produce three-dimensional h-MoO_3 rods and low-dimensional radial fibrous α-MoO_3 nanobelts by controlling only the holding time and acidity coefficient. The morphologies, phase evolution process of synthesized polymorphous MoO_3 were characterized and investigated by X-ray diffraction (XRD), scanning electron microscopy (SEM). The electrochemical properties of MoO_3 used as anode electrode in lithium batteries are presented.

2. EXPERIMENTAL

2.1 Synthesis procedure

All of the raw materials used in the study, including ammonium heptamolybdate (AHM), nitric acid (HNO_3), absolute ethyl alcohol, are of analytical grade and used as received. The synthesis process consisted of the following. First, AHM was dissolved in deionized water to form a saturated solution using an ultrasonic mixer at 25 ℃ for 30 min. Subsequently, 2.2 mol/l of HNO_3 was added to the AHM saturated solution to adjust the acidity coefficient at pH 1. In this study, the acidity coefficient is defined as the mole ratio of the HNO_3 and AHM in the solution. The mixtures were transferred to a stainless steel reactor. The reactor was tightly closed and heated at 180 ℃ for different times in an electric oven to affect the hydrothermal reaction. Finally, hydrothermal product was separated by filtration, washed with 33% HNO_3, deionized water，absolute ethyl alcohol, and dried at 65 ℃ in an electric oven for 6h.

2.2 Product characterization

The phase structure of hydrothermal products was characterized using a D8 X-ray diffractometer employing CuKα radiation at 45 kV and 35 mA with a scanning rate of 2°/min ranging from 10°-80°. The phase morphology was investigated using a scanning electron microscope (JSM-5610LV) and a high-resolution transmission electron microscope (HTEM, JEM-2100).

2.3 Anode electrode preparation, battery assembly and testing

All of the materials used to prepare anode electrode and battery assembly, including aluminum foil (t=0.02 mm), acetylene black, N-Methyl pyrrolidone (NMP), polyvinylidene fluoride (PVDF), are of analytical grade and used as received. The hydrothermal MoO_3 product was used for form the positive electrode material. The ratio of MoO_3, acetylene black and PVDF used to fabricate the electrode materials was 8:1:1. The anode electrode was fabricated as follows; first, the MoO_3 powder and acetylene black were mixed uniformly in an agate mortar. Second, PVDF was dissolved in NMP solution, based on a ratio of 0.1g PVDF to 10 ml NMP. Third, the mixture of the MoO_3 powder and acetylene black were slowly added to the clear solution with continuous stirring for 4-8 h to form the black mass which was then uniformly coated onto aluminum foil to prepare the anode electrode. Finally, the anode electrode was dried in an electric oven at 70 ℃ for 8 h and in a vacuum drying oven at 120 °C for 8 h. The dried anode electrode was cut into small round pieces with Φ15.8 mm × (20-30) μm for used. Lithium metal served as the battery cathode, cigard2400 micropore polypropylene screen was used as the separator in the battery and 1.0 $mol\bullet l^{-1}$ $LiPF_6$ was used as electrolyte of battery. The experimental battery was assembled in the glove box under Ar gas. The electrochemical properties of the assembly batteries were measured using a battery testing system (LanHe CT2001A) at the charge-discharge voltage of 1.0-4.0 V and ampere density of 0.5 $mA\bullet cm^{-2}$.

3. RESULTS AND DISCUSSION

3.1 Effect of hydrothermal reaction time

Fig. 1 displays the XRD spectrums of the synthetic products produced with an acidity coefficient of 5 for pH 1 and reaction temperature of 180℃ for various reaction times. The results indicate that the synthetic products were h-MoO_3 phase with no α-MoO_3 being identified. It is also evident that the intensities in the three planes of the h-MoO_3 family were higher than those of the standard powders, which are the (h10), (h00) and (h20) lattice planes for example (110), (210), (200), (300), (220), (320) et al. The three family planes reveal that the h-MoO_3 phase can be indexed as being highly anisotropic hexagonal symmetry.

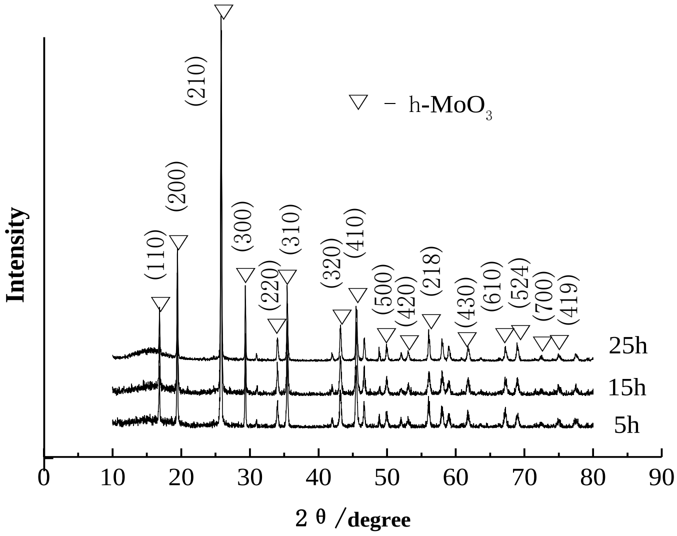

Figure 1. XRD spectrums of synthetic products under different reaction time

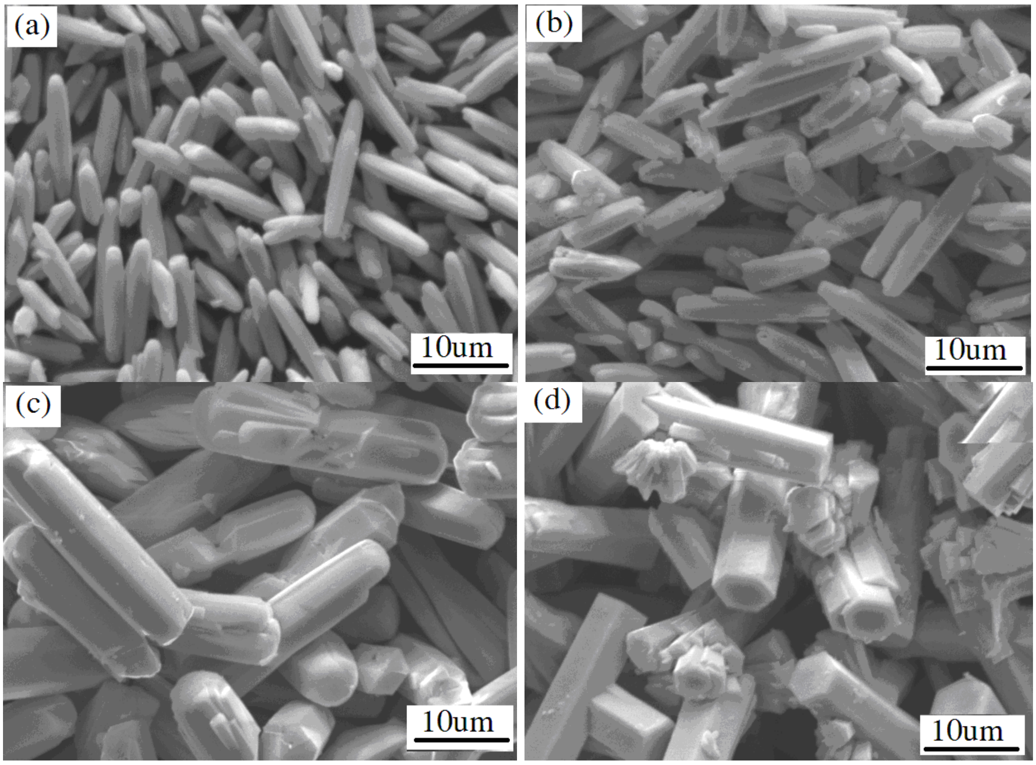

Figure 2. SEM images of h-MoO_3 under different time for (a) 2 h, (b) 6 h, (c) 20 h and (d) 25 h

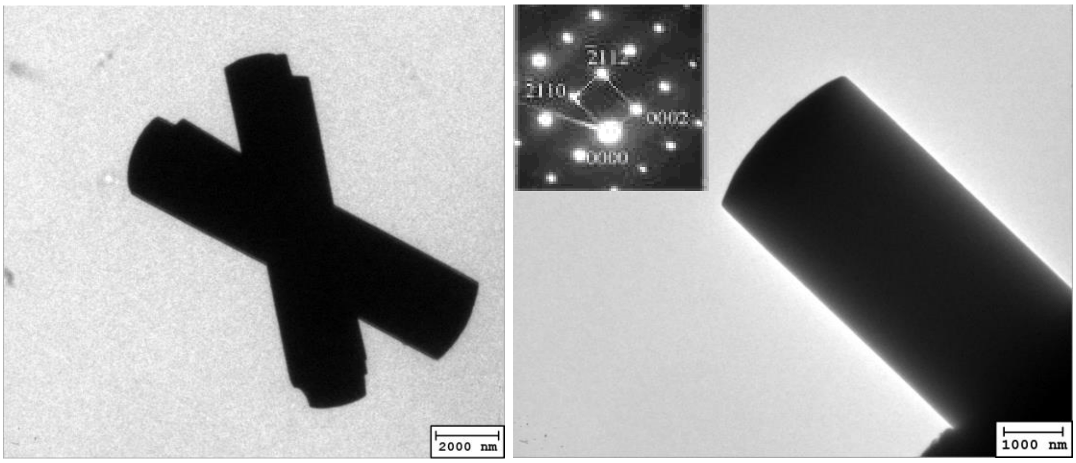

Figure 3. HTEM and SAED images of h-MoO_3 rods after holding time for 25 h at the acidity coefficient of 5 for pH 1 and reaction temperature of 180℃

The SEM images of the h-MoO_3 produced at different reaction times are shown in Fig. 2. The MoO_3 morphology exhibits shuttle-like rods with a smooth surface at the initial stage of reaction (~2 h). In the middle of hydrothermal reaction time (about 6 h), as the MoO_3 rods grew longer, crystal prisms began to be appear in the direction of the length. The h-MoO_3 morphology exhibited a similar irregular cylinder with the length of about 10-12 μm. At about 10-20 h of reaction time, the morphologies of irregular cylinders disappeared and hexagonal prototypes gradually evolved. After a prolonging reaction time of 25 h, the shape of the straight hexagonal micron rods was fully developed with smooth surfaces, the length of which was 15-20 μm and the diameter was 2-4 μm. Combined with TEM images and the diffraction patterns (see Fig. 4), it can be seen that the synthetic product was the pure h-MoO_3 phase, with a micron rod morphology. Thus, it can be concluded that the reaction time was not the key factor in development of the product's phase and did not cause the phase transition to occur happen in the low acidity coefficient conditions. As the reaction time increased, the h-MoO_3 phase became coarsened with regular growth.

3.2 Effect of acidity coefficient

Fig. 4 displays the XRD spectrums of the synthetic products at a reaction temperature of 180℃ for 25 h with different solution acidity coefficients. As the acidity coefficient increased from 5 to 30, diffraction peaks for α-MoO_3 gradually appeared and the h-MoO_3 phase diffraction peaks gradually weakened and disappeared. The XRD pattern also shows that diffraction peaks of (0k0) crystal faces, where k= 2, 4, 6, 10, are much stronger than the rest, which means that the products are significant anisotropy and a preferential growth occurred in a direction in the crystal formation process. These results suggest that the acidity coefficients played an important role in the evolution of the phase of the MoO_3.

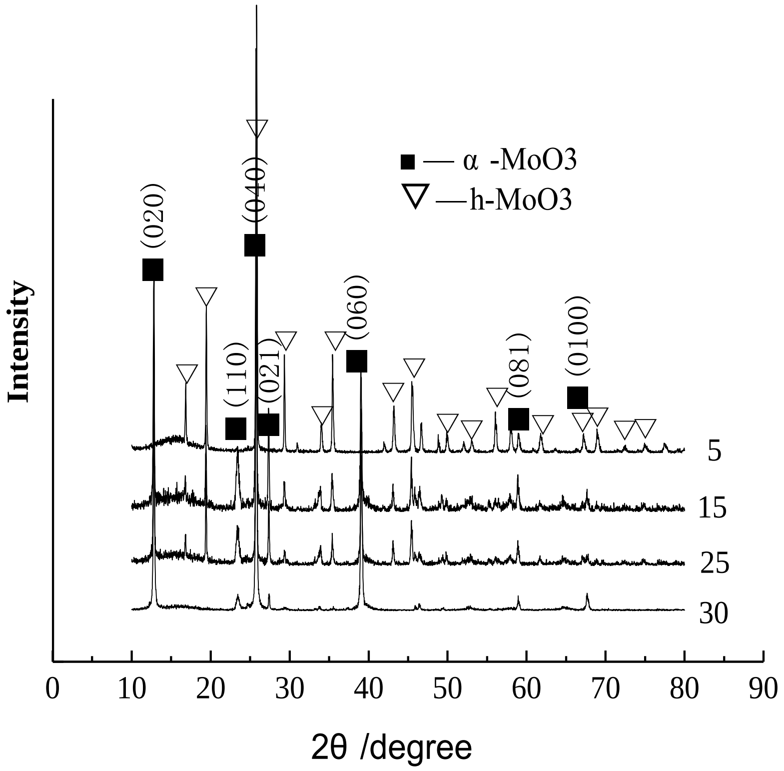

Figure 4. XRD spectrums of synthetic products under different acidity coefficients

Fig. 5 shows the SEM images of the MoO_3 phase as a function of the variation in the solution acidity coefficient. A significant change in the morphology of the MoO_3 product from three-dimensional hexagonal micron rods to low-dimensional nanobelts can be clearly observed. At a low acidity coefficient of 5, the morphology appeared to be the typical micron-sized h-MoO_3 rods. As the acidity coefficient was increased to 10-15, the micron-sized h-MoO_3 rods began to become more fine, short and grainy in texture. In addition, some belts morphology can also be seen. Corresponding to the XRD pattern, the α-MoO_3 phase is evident. Furthermore, with a further increase in the acidity coefficient, the fine-grained h-MoO_3 phase gradually disappeared and thinner, long belts or fibrous α-MoO_3 phases emerged. When the acidity coefficient reached 30, the product grew rapidly and was converted to α-MoO_3 nanobelts in place of the h-MoO_3 phase. The α-MoO_3 nanobelts exhibited a length of 20-30 μm and a diameter of 100-300 nm.

Fig. 6 displays TEM images of the α-MoO_3 product synthesized with an acidity coefficient of 30. It can be seen that the α-MoO_3 exhibited disorder and randomly-sized, smooth nanobelts. The SAED at the top of Fig. 6-b verifies that the direction of growth was parallel to the axial direction of the nanobelts. Furthermore, the lattice finger images of the α-MoO_3 at the bottom of Fig. 6b can be clearly seen in the HTEM images. The adjacent interplanar spacing corresponds to the spacing of the (200) lattice plane. According to Bravis law, actual crystal faces are often parallel to the crystal planes with the largest atom density [19]. The interplanar spacing is larger, the force of crystal faces attracting external particles in the vertical direction is weaker. In orthorhombic phase α-MoO_3, (0k0) crystal planes are the largest atom density planes. So the synthesized samples grew in the [001] direction and formed α-MoO_3 phase.

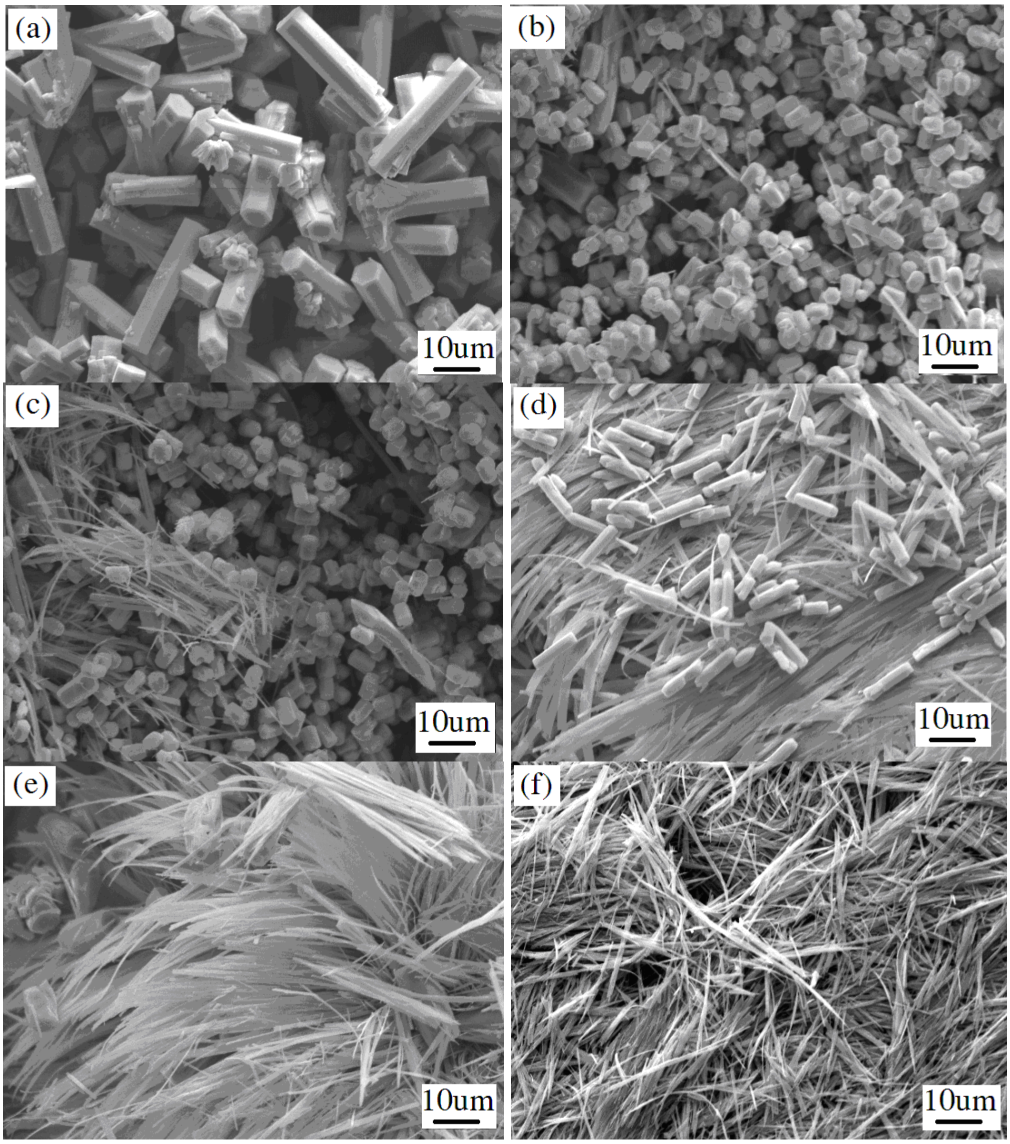

Figure 5. SEM images of α-MoO_3 phase obtained at acidity coefficients of (a) 5, (b) 10, (c) 15, (d) 20, (e) 25, (f) 30

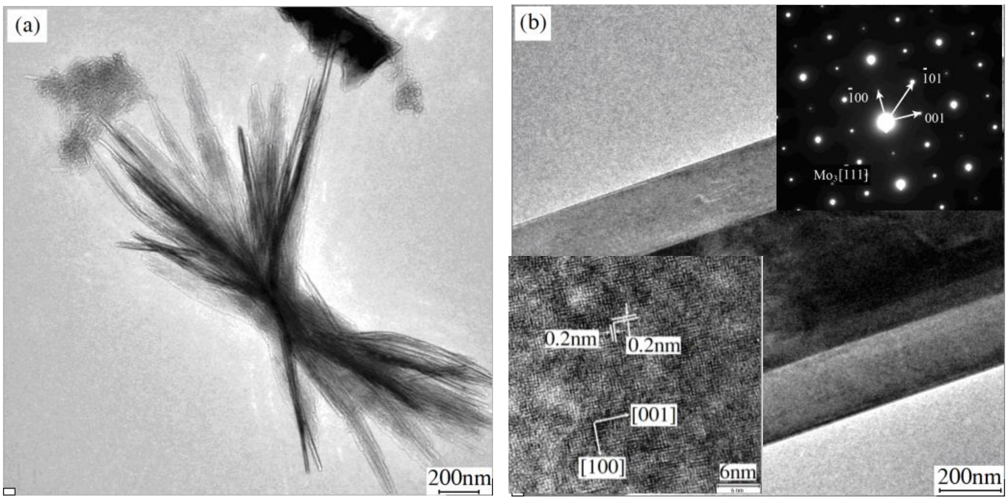

Figure 6. TEM images of the α-MoO_3 phase (a) morphology and (b) HTEM and SAED

3.3 Formation mechanism

The polymorphous MoO_3 phases produced by the hydrothermal synthesis can be identified as a dissolve-recrystallization process. The mechanism for the formation of MoO_3 from isopolymolybdate $(Mo_7O_{24})^{6-}$ anions in a hydrothermal synthesis have been reported to be as follows [20]:

$Mo_7O_{24}^{6-} + 6H^+ \rightarrow 7MoO_3 + 3H_2O$

The growth process was reported to be summarized as:

$Mo_7O_{24}^{6-} + 6H^+ + 11H_2O \rightarrow 7MoO_3 \cdot 2H_2O$

$MoO_3 \cdot 2H_2O \rightarrow MoO_3 \cdot H_2O + H_2O$

$\alpha\text{-}MoO_3 \cdot H_2O \rightarrow MoO_3 + H_2O$

In the overall equilibrium shown above, high concentrations of both $Mo_7O_{24}^{6-}$ and H^+ shift the reaction to the right. It has also been suggested that the formation and phase structure of MoO_3 have a strong dependence on the acid concentration (acidity coefficient) of solution and the reaction time.

It has been found that the growth unit of the MoO_3 is the $[MoO_6]$ octahedron (see Fig.7-a). In the acid solution, when the acidity coefficient was 5, the driving force was low, because of the lower H^+ concentration. Therefore, few growth units were created and there was a detriment to growth at the crystal-liquid interface. In addition, based on the growth pattern of the anion coordination-polyhedra, the velocity of growth of the negative polar plane could not be controlled, because few H^+ ions were adsorbed at the negative polar plane of the MoO_6 octahedron. Thus, the corner to corner growth became the basis of the growth unit and it easily developed into a network shaped hexagonal MoO_3 phase (see Fig.7-b). The formation mechanism of the h-MoO_3 has been also described that a substantial amount of oxygen groups such as –COOH and –OH (few of H^+ ions), which are easy to hold MoO_3 particles on the same surface; the surface would scroll up to a rod with the formation of Mo–O bond due to its flexibility. As the temperature and holding time increase, the rod gradually grows up and finally forms h-MoO_3 [21].

With the increase of the acidity coefficient, the concentration of H^+ ions increased and the stronger driving force was beneficial to the nucleation and growth of growth units. At the same time, the growth of the negative polar plane was blocked, because more and more H^+ ions were adsorbed at the negative polar plane. Thus, the velocity of the positive polar plane was far greater than the others. Therefore, the growth was changed to superposition by sharing the edges and by sharing the corners of the positive polar plane structure, which developed into an orthorhombic MoO_3 phase (see Fig.7-c).

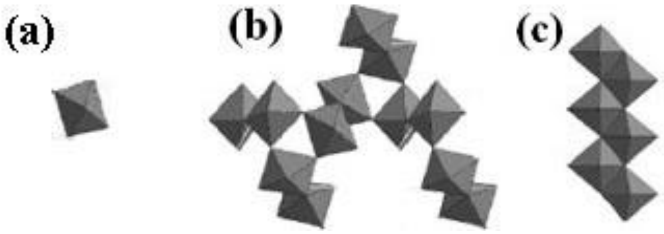

Figure 7. growth of MoO_3: (a) growth unit of $[MoO_6]$, (b) connected by corner (h-MoO_3) and (c) superposition of growth unit (α-MoO_3)

3.4 Electrochemical properties of polymorphous MoO_3

Table 1 exhibited the specific capacity and cycling properties of both types of MoO_3 phases. The initial discharge curve of the battery containing the synthesized h-MoO_3 is displayed in Fig.8. It can be seen that the initial discharge capacity of h-MoO_3 phase was 171.4mAh·g^{-1} and a discharge plateau occurred at about 2.0 V. However, it appeared that there was an obvious improvement in the α-MoO_3 phase. The initial discharge capacity was at about 223.1mAh·g^{-1} and a wide and even plateau emerged at about 2.2 V. With the increase of the cycling index, the specific capacities of both types of MoO_3 phases gradually declined. After cycling 20, the specific capacities of the h-MoO_3 and α-MoO_3 phases dropped to 95.7 mAh·g-^{1} and 135.3 mAh·g^{-1}. The capacity retention ratios of the h-MoO_3 and α-MoO_3 phases were approximately 55.8% and 60.6%.

Table 1. Specific capacity of α-MoO_3 and h-MoO_3 at the initial 20 cycles

cycle index	1	2	3	4	5	6	7	8	9	10
h-MoO_3	171.4	169.3	168.3	165.5	164.3	163.7	160.6	157.4	155.6	150.5
α-MoO_3	223.1	215.6	200.5	199.3	195.7	194.7	186.3	186	180.6	172.3
cycle index	**11**	**12**	**13**	**14**	**15**	**16**	**17**	**18**	**19**	**20**
h-MoO_3	144.5	142.9	135.7	134.8	130.5	126.2	120.6	113.7	105.9	95.7
α-MoO_3	165.3	163.2	156.9	152.6	150.7	149.2	147.5	146.2	140.8	135.3

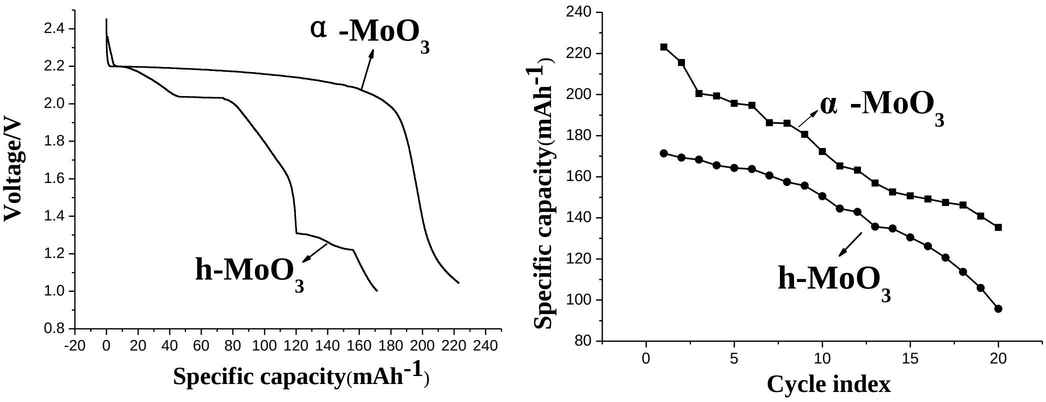

Figure 8. Initial discharge curve and cycling curve for the various MoO_3 phases

It can determinate that from these reported electrochemical performance results the electrochemical properties (initial discharge capacity and cycling capacity) of the α-MoO_3 phase were better than the h-MoO_3 phase. In other words, the electrochemical properties were depended on the phase of the MoO_3. The nanofibrous morphology reveals more active crystallographic (010) planes, which will make the intercalation and deintercalation of Li^+ ions very easy. Moreover, it has been demonstrated that the Li^+ intercalation takes place in the van der Waals spacing preferentially at the (010) plane [22]. Therefore, the α-MoO_3 phase with a thin fibrous morphology not only provided a shorter migration path for the electrons and Li^+ ion, but also increased the contact area between the electrode and electrolyte. However, hexagonal h-MoO_3 is a metastable phase, which is constructed by using the zigzag chains of [MoO_6] octahedra as the building blocks connecting through adjacent oxygens. Although the tunnel structure of h-MoO_3 could result in electron–hole separation and provide locations for cation insertion and extraction, the exposed (010) planes are less than that of the MoO_3 nanofibrous, leading to their less capacitances [23].

Fig. 9 displays the cyclic voltammetry curve of the α-MoO_3 positive electrode materials. Two distinct and sharp peaks appeared at 2.0 V and 2.15 V for the oxidation peaks, and at 1.85 V and 1.95 V for the reduction peaks. Two pairs of symmetrical peaks corresponding to the intercalation/deintercalation of Li^+ ion indicated that the electrode reaction was reversibly. The two peaks on the reduction curve indicated that the Li^+ intercalation process in the α-MoO_3 materials was accomplished in two steps. The first step was the Li^+ embedding into the [MoO_6] octahedron and the second step was the movement of the actions into the layers of the [MoO_6] octahedron. The potential difference between the oxidation peaks and the reduction peaks resulted from the concentration polarization on the electrode surface. On the other hand, there was a variation between the reduction peaks (1.85V and 1.95V in Fig.9) and the discharge plateau (2.0 V in Fig.8). The first reason for this was the difference in the test process. The cyclic voltammetry method is a potentiostatic technique where the voltage is controlled and the current is allowed to float. By contrast, the charge-discharge test is a galvanostatic technique where the current is held constant and the voltage of the electrode is allowed to float. Another reason for this discrepancy is centered on the button battery used for the testing, which was twin-electrode system, where both the counter electrode and reference electrode were lithium.

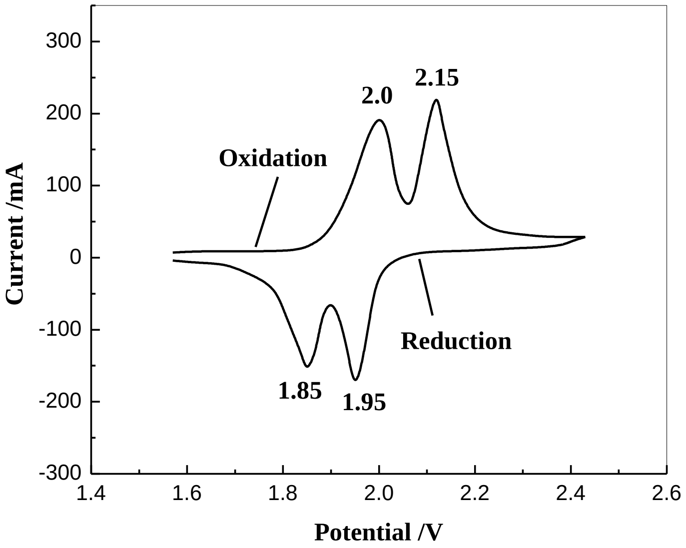

Figure 9. the cyclic voltammetry curve of the α-MoO_3 phase

Electrode polarization could have occurred at the reference electrode when the current was varied during the tests. As a result, the variation in the current in the cyclic voltammetry method and the charge-discharge method could lead to a variation in the electrode polarization. This would explain in the deviation between the reduction peaks and the discharge platform could be generated. In addition, although the electrochemical performances are correspond to the nanofibers which delivered a capacity 265 mAh•g^{-1} for the first discharge in the potential range 3.5-1.5 V, there are still quite grate difference in compare to the capacity of 600 mAh•g^{-1} for α-MoO_3 electrode using CMC binder [24]. Because CMC (sodium salt of carboxy methyl cellulose) provides better electrode stability towards conversion reaction in compare to PVDF binder.

4. CONCLUSION

In this study, h-MoO_3 and α-MoO_3 were prepared using a facile hydrothermal synthesis. Although both the hydrothermal reaction time and the solution acidity coefficient were found to play important roles in controlling the crystalline structure and morphology of the product MoO_3, the acidity coefficient was the critical factor, which determined the number of growth units and the crystal structure. At the lower acidity, the poor number of growth units and the driving force led to developing the h-MoO_3 micro rods with the length of 15-20 μm and the diameter of 2-4 μm as the holding time increased. With the increase of the acidity coefficient, the phase structure and phase morphologies evolved and the α-MoO_3 nanobelts with the length of 20-30 μm and a diameter of 100-300 nm replaced the h-MoO_3 micron rods in the product. Both the h-MoO_3 and α-MoO_3 possessed electrochemical activity. The initial discharge capacity of h-MoO_3 and α-MoO_3 were 171.4 mAh•g^{-1} and 223.1 mAh·g^{-1} and after 20 cycles the capacity retention ratios were 55.8％ and 60.6%. The specific capacity and cycling properties of α-MoO_3 phase were better than the h-MoO_3 phase.

ACKNOWLEDGEMENT
This work is supported by National Natural Science Foundation of China (No.50972039) and Program for Changjiang Scholars and Innovative Research Team in University (No.IRT1234).

Reference

1. Gil-Su Kim, Young Jung Lee, Dae-Gun Kim, Young Do Kim, *Journal of Alloys and Compounds,* 454 (2008) 327–330.
2. Beatriz Mendoza-Sáncheza, Thierry Brousseb, Claudia Ramirez-Castrob, Valeria Nicolosia, Patrick S. Grant, *Electrochimica Acta*, 91 (2013) 253– 260.
3. ShigehitoDeki, Alexis Bienvenu Beleke, Yuki Kotani, Minoru Mizuhata, *Journal of Solid State Chemistry*, 182 (2009) 2362–2367.
4. R. Pandeeswari, B.G. Jeyaprakash, *Biosensors and Bioelectronics*, 53 (2014) 182–186.
5. Reddeppa Nadimicherla, Wen Chen, Xin Guo, *Materials Research Bulletin,* 66 (2015) 140–146.
6. A. Chithambararaj, A. Chandra Bose, *Journal of Alloys and Compounds*, 509 (2011) 8105– 8110.
7. C.V. Ramanaa, V.V. Atuchin, I.B. Troitskaia, S.A. Gromilov, V.G. Kostrovsky, G.B, *Solid State Communications*, 149 (2009) 6-9.
8. Zheng L, Xu Y, Jin D, Xie Y. *Chem Mater*, 2009;21:5681–90..
9. S. Rajagopal, D. Nataraj, O.Y. Khyzhun, Yahia Djaoued, Jacques Robichaud, Chang-Koo Kim, *Materials Chemistry and Physics,* 141 (2013) 383-392.
10. G.R. Li, Z.L. Wang, F.L. Zheng, Y.N. Ou, Y.X. Tong, *J. Mater. Chem*., 21 (2011) 4217.

11. K Shiva, HB Rajendra, KS Subrahmanyam, AJ Bhattacharyya, CNR Rao, *Chemistry–A European Journal*, 2012, 18 (15), 4489-4494.
12. Konda Shiva, H.S.S. Ramakrishna Matte, H.B. Rajendra, Aninda J. Bhattacharyya, C.N.R. Rao, *Nano Energy*, (2013) 2, 787–793.
13. Zhuangzhi Wu, Dezhi Wang, Xun Liang, Aokui Sun, *Ultrasonics Sonochemistry*, 18 (2011) 288–292.
14. Shouzhu Lia, Changlu Shaoa, Yichun Liua, Shanshan Tanga, Rixiang Mu, *Journal of Physics and Chemistry of Solids*, 67 (2006) 1869-1872.
15. H. Sinaim, Dong Jinham, Jae sunglee, A. phuruangrat, S. Thongtem, T. thongtem, *Journal of Alloys and Compounds*, 516 (2012) 172-178.
16. Bin Gao, Huiqing Fan, Xiaojun Zhang, *Journal of Physics and Chemistry of Solids*, 73 (2012) 423-429.
17. Xia Zhang, Min Yang, Xianzhong Zeng, Yanxing Qi, *Materials Letters*, 109 (2013) 120-123.
18. Uttam Kumar Sen, Sagar Mitr, *Energy Procedia*, 54 (2014) 740-747.
19. Ichiro Sunagawa, *Morphology of crystals part A*, Terra Scientific Publishing Company, Tokyo, 1987.
20. X.M. Sun, X. Chen, Z.X. Deng, Y.D. Li, Mater. *Chem. Phys.*, 78 (2002) 99–104.
21. Qiwei Tang, Li Wang, Kunlei Zhu, Zhongqiang Shan, Xue Qin, *Materials Letters*, 100 (2013) 127–129.
22. Jin Li, Xiaoheng Liu. *Materials Letters*, 112 (2013) 39–42.
23. Xia Zhang, Min Yang, Xianzhong Zeng, Yanxing Qi, *Materials Letters*, 109 (2013) 120–123.
24. A.M. Hashem, H. Groult, A. Mauger, K. Zaghib, C.M. Julien, Journal of Power Sources, 219 (2012) 126-132.

© 2017 The Authors. Published by ESG (www.electrochemsci.org). This article is an open access article distributed under the terms and conditions of the Creative Commons Attribution license (http://creativecommons.org/licenses/by/4.0/).